Iraqi Journal of Science

ISSN: 0067-2904

A Novel Approach for Synthesizing the Pan-chromatic Band to (10 m) of Landsat 9 Based on Sentinel-2 Data to Improve Classification Performance

Nehad Hameed*, Taghreed Abdalhameed Naji

Department of Physics, College of Education for Pure Science Ibn-Al-Haitham, University of Baghdad, Baghdad, Iraq

Received: 10/3 /2024 Accepted: 20/6/2024 Published: 30/5/2025

Abstract

This study investigates the impact of spatial resolution enhancement on supervised classification accuracy using Landsat 9 satellite imagery, achieved through pan-sharpening techniques leveraging Sentinel-2 data. Various methods were employed to synthesize a panchromatic (PAN) band from Sentinel-2 data, including dimension reduction algorithms and weighted averages based on correlation coefficients and standard deviation. Three pan-sharpening algorithms (Gram-Schmidt, Principal Components Analysis, Nearest Neighbour Diffusion) were employed, and their efficacy was assessed using seven fidelity criteria. Classification tasks were performed utilizing Support Vector Machine and Maximum Likelihood algorithms. Results reveal that specific synthetic PAN bands, notably PAN10, PAN2, and PAN9, demonstrate superior performance in image fusion and classification tasks. This study underscores the significance of selecting fusion algorithms and panchromatic bands tailored to applications, with Support Vector Machine classifiers showcasing resilience across diverse fusion methods. Even though the PAN8 band has exhibited lower overall accuracy, it is helpful in effectively delineating some land cover classes.

Keywords: *SVM classifier, fusion, panchromatic band, Landsat 9, Sentinel 2.*

طريقة جديدة لتجميع النطاق اللوني الشامل (*PAN*) إلى (10 م) لحزم *Landsat 9* بناءً على بيانات *Sentinel-2* لتحسين أداء التصنيف

نهاد حميد*, تغريد عبد الحميد ناجي

قسم الفيزياء، كلية التربية للعلوم الصرفة ابن الهيثم، جامعة بغداد، بغداد، العراق

*Email: nohad.hameed1104a@ihcoedu.uobaghdad.edu.iq

الخلاصة

تبحث هذه الدراسة في تأثير تحسين الاستبانة المكانية على دقة التصنيف الخاضعة للإشراف لصور القمر الصناعي لاندسات 9، والتي تم تحقيقها من خلال تقنيات الشحذ العام بالاستفادة من بيانات Sentinel 2. تم استخدام طرق مختلفة لتجميع نطاق بانكروماتي (PAN) من بيانات Sentinel 2، بما في ذلك خوارزميات تقليل الأبعاد والمتوسطات المرجحة بناء على معاملات الارتباط والانحراف المعياري. تم استخدام ثلاث خوارزميات للشحذ الشامل (غرام شميدت، تحليل المكونات الرئيسية، انتشار أقرب جار)، وتم تقييم فعاليتها باستخدام سبعة معايير للدقة. تم تنفيذ مهام التصنيف باستخدام خوارزميات آلة متجه الدعم وخوارزمية الاحتمال الأقصى. تكشف النتائج أن نطاقات PAN الاصطناعية المحددة، ولا سيما PAN10 وPAN2 وPAN9، تظهر أداء فائقا في كل من مهام دمج الصور والتصنيف. تؤكد هذه الدراسة على أهمية اختيار خوارزميات الاندماج والنطاقات البانكروماتية المصممة خصيصا لتطبيقات معينة، مع مصنفات الة متجه الدعم التي تظهر المرونة عبر طرق الاندماج المتنوعة. على الرغم من أن نطاق PAN8 قد أظهر دقة إجمالية أقل ولكنه مفيد في تحديد بعض فئات الغطاء الأرضي بشكل فعال.

1. Introduction

Land use and land cover (LULC) information is paramount in various geospatial applications, such as regional administration, urban planning, and environmental management [1, 2]. The LULC is critical for comprehending the intricate interplay between humans and their environment. Land Cover encompasses the physical attributes of the Earth's surface, including vegetation, soil, and water, while Land Use delineates human activities and purposes for utilizing the LC [3]. Developing accurate maps of LULC classification is vital for collecting valuable information about these applications [4-6].

In this era, remote sensing data has become one of the most important sources of information about the earth’s cover by various satellite platforms due to its availability and continuity [7].

The Landsat program, known for its long-standing history, has significantly impacted Earth observation with its continuous imaging program from space. Landsat-9, equipped with (OLI-2), captures a high dynamic range (14-bit) and the Thermal Infrared Sensor (TIRS). This enhanced radiometric resolution of OLI-2 provides higher sensitivity, opening new frontiers in the field and facilitating global mapping [8-11].

The Sentinel-2 mission aimed to provide high spatial resolution wide-swath satellite data for diverse applications and complement other missions. It shares similar wavelengths and the same geographic coordinate system with Landsat data, making it an excellent opportunity to combine these two types of satellite data [12, 13]. All Landsat Sentinel-2 data are available to users under the free and open data policy [14, 15]; one of the drawbacks of the sentinel-2 satellites is that they lack the panchromatic (Pan) band [16].

The panchromatic (Pan) band is usually recorded with the maximum spatial resolution allowed by the satellite sensor and the transmission's ability of the data link, so it provides a detailed geometric feature. On the other side, the multispectral (MS) bands are collected with

a lower spatial resolution (half or quarter of resolution) due to the constraints of signal-to-noise ratio and the transmission ability of data link, with higher spectral resolution [17].

Increasing both spectral and spatial resolutions is fundamental for refining mapping accuracy. However, fusing remote sensing data collected using different sensors is challenging [18]. Several requirements must be achieved, and the fusing should be carefully performed, pixel size must be unified, and images should be co-registered [19, 20]. Integrating multi-sensor images by fusion can provide higher-quality images than those from one platform [21, 22]. In contrast to the challenge of fusing data from multiple sensors, pan-sharpening with a single sensor does not require image-to-image registration [23]. The MS bands fused with PAN bands to enhance the spatial resolution using the pan-sharpening process, which is essential in many mapping and remote sensing applications [17, 24, 25].

The component substitution (CS) algorithms family comprises many widespread pan-sharpening methods [26], including the Gram-Schmidt method (GS) and the principle component method (PC) [27]. One of the most widely used algorithms is the Gram-Schmidt method. It performs better than most pan-sharpen methods in enhancing image sharpness and reducing color distortion [22, 28]. The principal component analysis PC rotates multispectral data into principal components, replacing the first PC with the PAN band to enhance image sharpness and spectral information in subsequent PCs. It executes a multidimensional coordinate system rotation to convert the original inter-correlated bands into a new set of uncorrelated PCs [29, 30]. The nearest-neighbor diffusion (NN) is a multi-resolution analysis (MRA) method that employs a weighted linear combination of various bands in the neighboring pixels.to enhance spatial details while maintaining spectral quality [31, 32].

In this work, three data-dimensional reduction methods were employed to extract synthesized panchromatic (PAN) bands from the four (10 m) Sentinel-2 bands, along with selecting individual bands, the average of the four bands, and the weighted average of the four bands depending on the correlation coefficient (r) between Landsat-9 bands and the four Sentinel-2 bands and the standard deviation (s) values of the Sentinel 2 bands.

Dimensionality reduction converts the data into a lower-dimensional space. It is a helpful way to remove unnecessary variation in the data and extract lower dimensions [33], such as the analysis of the independent components (ICA), the non-negative matrix factorization (NMF), and Gram -Schmidt transformation (GST) [34-36]. Several metrics were used to assess the fused image quality, including root mean square error (RMSE) [37, 38], spectral angle mapper (SAM)[39], relative global-dimensional synthesis error (ERGAS) [40] Peak signal-to-noise ratio (PSNR)[41-43], correlation coefficient (r), structural similarity index (SSIM) [44], and universal image quality index (UIQI) [45]. These indicators have been widely used to evaluate the performance of the data fusion algorithms.

Satellite image classification is one of the main tasks of remote sensing applications. Remote sensing image classification accuracy is enhanced when several data sources are used in the processing [46]. Indeed, due to the similarity in spectral characteristics among different surface types [47], the utilization of powerful classification algorithms becomes essential. Support vector machine (SVM) is a popular nonparametric supervised machine learning algorithm for digital image classification because it can deal with nonlinear classification situations using a small number of samples [48, 49]. The SVM approach is a statistical

learning theory. This technique determines the location of decision boundaries, which creates the best separation of the image classes [50, 51]. Compared with many existing classifiers, the SVM classifier can attain competitive results using small training samples [52, 53]. This characteristic is essential for precision classifications, as acquiring ground truth data proves costly, daunting, and time-consuming, necessitating field surveys and laboratory experiments [53]. The maximum likelihood (ML) classifier, one of the most common classifiers used in remote sensing applications, hinges on assumptions of normal distribution, equal covariance, and sufficient training samples [54, 55].

Bouslihim and his coauthors in 2022 [56] compare the performance of pan-sharpened Landsat 9 and Sentinel-2 imagery for land-use classification using machine-learning classifiers. The researchers Mansourmoghaddam, Mohammad, et al. 2022 [57] evaluate the Sentinel-2, Landsat-8, and their fused images' efficacy in enhancing the LC map accuracy for Yazd, Iran, by using the Gram-Schmidt technique, a primarily spatial fusion of Landsat-8 images with Sentinel-2 images. Similarly, Sigurdsson, Jakob, et al. 2022 [58] adopted a similar approach by fusing data from Copernicus Sentinel-2 (S2) and Landsat 8 (L8) satellites. The researchers Ali, Zahraa R. and Muhaimeed, Ahmad S. 2016 [6] used Sentinel-2 data to classify land cover in Baghdad City, Iraq. They used a support vector machine (SVM) classifier to classify the data into seven land cover classes: water, built-up, vegetation, bare land, soil, salt-affected land, and rocks. Thanh Noi, Phan, and Martin Kappas 2018 [59] compared the performance of three machine learning classifiers - random forest (RF), k-nearest neighbors (kNN), and support vector machines (SVM) for land use/cover classification using Sentinel-2 image data. Topaloğlu, R.H. et al.,2016 [60] classified the land cover of Istanbul city using both maximum likelihood and support vector machine classifiers for two datasets after making geometric corrections to them. The first is a dataset from the Landsat 8 satellite with a resolution of 30 m, and the second is collected from similar bands of the Sentinel-2 satellite after resampling it from 10 and 20 m to 30 m. The work conducted by researchers [61-64] used the computation of overall accuracy based on the confusion matrix to evaluate the classification results.

Rimal, Bhagawat Rijal, Sushila Kunwar, and Ripu 2020 [65] discovered that the Support Vector Machine (SVM) classifier outperformed the Machine Learning classifier regarding user and producer accuracies. Additionally, SVM demonstrated effectiveness in land cover classification.

Abdulwahab et al. (2023)[66] used three pan sharpening techniques to enhance the spatial resolution of 175 hyperon bands from 30 to 15m using LS9 PAN. They used Principal Components Analysis (PC), the Gram-Schmidt algorithm (GS), and Nearest Neighbour Diffusion (NN). They reduce the dimensionality of the hyperspectral data using the MNF transformation. They found that PC and GS performed similarly in preserving the spectrum and enhancing the details of the fused images, as judged by visual inspection. However, NN showed less improvement than the other two techniques.

This study aimed to identify the most effective methods for synthesizing PAN bands with a 10m spatial resolution from Sentinel-2's four 10m bands. When used to fuse Landsat 9 data, how these extracted bands affect the overall accuracy of land cover classification compared

to using the original Landsat 9 bands directly was investigated. If land cover classification based on these fused bands delivers higher accuracy than the original bands, it would demonstrate the study's success. Additionally, it aimed to provide recommendations for combining specific fusion methods and classification algorithms based on the achieved accuracy.

2. Data and methods

2.1 Data sources

The satellite imagery from Landsat-9 OLI/TIRS C2 L2 and Sentinel-2A MSI were used. The Landsat 9 OLI C2 L2 collection provides global surface reflectance products [67]. The satellite scene data of the study site were extracted from the original scene identified by LANDSAT_PRODUCT_ID= "LC09_L2SP_168037_20231018_20231019_02_T1". The scene center time was recorded at "07:33:52.2487420Z".

The Landsat-9 satellite has two instruments: the Operational Land Imager 2 (OLI-2) and the Thermal Infrared Sensor (TIRS-2). The Landsat-9 consists of 11 channels (dynamic range 14-bit), the first seven channels being multispectral (visible, near-infrared, shortwave infrared) recorded at 30 m spatial resolution. The eighth band is panchromatic, which has a resolution of 15 m. TIRS-2 consists of two thermal infrared channels with a spatial resolution of 100 m
[8-11, 68].

The panchromatic band was downloaded from LANDSAT_PRODUCT_ID= "LC09_L1TP_168037_202311018_20231019_02_T1" as it was not included in the Level 2 bundles. All the data (8 bands) were collected from the OLI-2 sensor. Band 9 (Cirrus) and TIRS-2 were neglected in this work. Landsat data was downloaded from https://earthexplorer.usgs.gov/.

Sentinel 2A data was acquired from the European Union's Earth observation program through https://dataspace.copernicus.eu/. Sentinel-2A was equipped with the Multispectral Imager (MSI), which consists of 13 channels with various spatial resolutions (10, 20, and 60 m) and wavelengths covering the visible, near-infrared, and shortwave infrared spectrums. However, Sentinel-2 does not have a conventional panchromatic band [15, 69]. Level-2A (surface reflectance, ortho-images in UTM/WGS84 projection) are available to users under a free and open data policy [14, 70]. The study region was extracted from the original scene with the ID: S2A_MSIL2A_20231018T074921_N0509_R135_T38SMB_20231018T113602.

The scene center time was recorded at 07:49:21.024Z. Only the four bands with 10m spatial resolution were used in this work.

Both satellite data are freely available worldwide and share the same geographic coordinate system, making it an excellent opportunity to combine these two types of satellite sensor data [12].

Both datasets were undergone geometric correction, ensuring accurate spatial representation. The atmospheric correction was also applied to convert the sensor radiance to surface reflectance. All these corrections, performed by the data providers, enhance the reliability of the datasets. However, it is essential to note that the panchromatic band (Band 8) of Landsat 9 is an exception and has not been atmospherically corrected by the data provider.

Table 1: The used satellite scenes

Satellite Scene	Spatial Resolutions	Date	Used bands	Scene Dimensions (Pixel)
Landsat 9_OLI	30&15 m	18 October 2023	Bands 1-7&8	(1000 × 1000)
Sentinel 2b	10 m	18 October 2023	Bands 2-4 & 8	(3000x3000)

2.2 Study area

The study area is located north of Baghdad City. It extends over parts of three governorates, covering parts of Baghdad, Salah al-Din, and Diyala governorates, and situated between the coordinates 42° 40’ 15.60" and 45° 40’ 15.60" longitude and 37° 12’ 35.28" and 37° 30’ 35.28" latitude, spanning 900 km². This predominantly agricultural area encompasses several small towns and cities, including Al-Mushahada, Al-Tarmiyah, Al-Abayji, and Al-Dujail on the right bank of the Tigris River. At the same time, the left bank features Mansouriya, Al-Saadiyah, Al-Sindiyah, Habhab, Al-Khalis, and Al-Ghalibiya. It poses residences scattered among orchards and farmlands. The river, coursing from north to south, is bordered by palm groves of varying densities and heights, interspersed with citrus trees. Many fish breeding ponds, varying in size, shape, and depth, are especially noticeable on the river’s right side, some of which are dry. Vineyards and fruit plantations distinguish the western and northwestern regions. The area showcases three types of farmlands: dry soil unprepared for agriculture, plowed land ready for winter cultivation, and lands covered with natural vegetation, which comprise a significant portion of the study area. The study area was derived from images of the Landsat-9 and Sentinel-2A satellites taken on 18 October 2023. This period marks a transitional phase between the end of the summer and the beginning of winter agricultural seasons; hence, many lands are either at the start of their preparation for winter season agriculture or at the termination of the summer season, with some lands cultivated with various types of fodder crops. The area also houses several greenhouses, but they were disregarded as they constitute less than 1% of the study area.

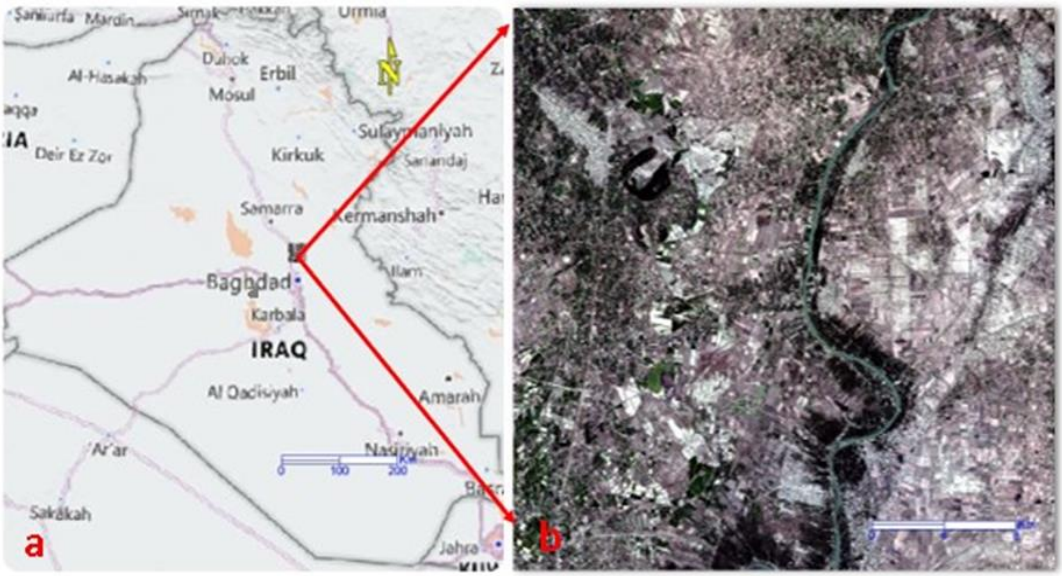

Figure 1 : a. Iraq's map with study region scene, and b. The natural color of Landsat-9 OLI for the selected study area from the original scene with path 167/row 038.

2.3. Methods

This study applied a pan-sharpening process to Landsat-9 satellite data to improve its spatial resolution to 10 m, based on four bands from the Sentinel-2A satellite (2, 3, 4, and 8), with a spatial resolution of 10 m. Since Sentinel-2A lacks a Panchromatic (Pan) band, several methods were used to simulate a Panchromatic (Pan) band, as listed in Table 2. These methods included using (1) applying dimension reduction algorithms, (2) using each of the four bands individually as PAN bands, (3) averaging the four bands eq. 1, and (4) calculating a weighted average based on the correlation coefficients (r)s and the standard deviation (ꙅ) of the four Sentinel 2 bands eqs. (2 [71], 3 [72],4, and 5).

$$\text{PAN9} = \frac{(SB2+SB3+SB4+SB8)}{4} \quad (1)$$

$$r = \frac{\sum_{i=1}^{n}(x_i-\bar{x})(y_i-\bar{y})}{\sqrt{\sum_{i=1}^{n}(x_i-\bar{x})^2 \sum_{i=1}^{n}(y_i-\bar{y})^2}} \quad (2)$$

$$\sigma = \sqrt{\frac{1}{N}\sum_{1}^{N}(x_i-\mu)^2} \quad (3)$$

$$w_n = \frac{\sum_{1}^{u} r}{u} \times \sigma \quad (4)$$

$$Normalized\ Band\ Weight = \frac{w_n}{\sum_{1}^{n} w_n} \quad (5)$$

w_n is the absolute weight for each of the four bands, *(r)* is the correlation coefficient between each band of the four Sentinel 2 bands (SB) and Landsat 9 bands (LSB), ꙅ is the standard deviation of each of the four Sentinel 2 bands (SB), *u*: is the number of Landsat bands, *and n*: is the number of Sentinel 2 bands.

Various software and programs were utilized in this study, including SNAP 6.00, ENVI 5.6, and Python 3.11. The overall processes are demonstrated by the flowchart Fig.2.

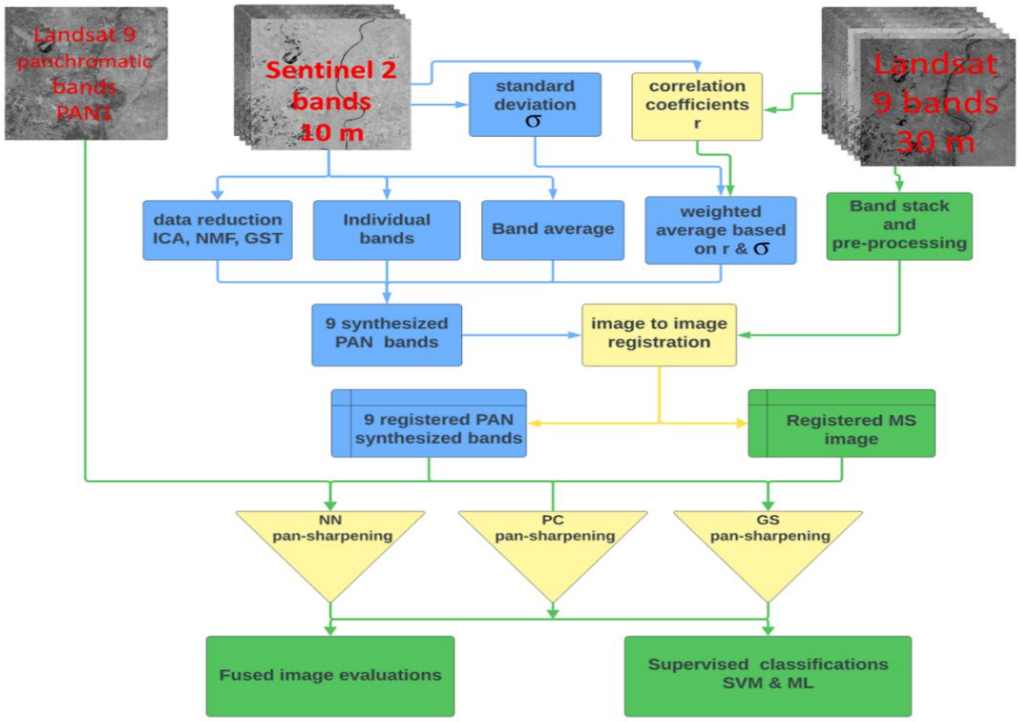

Figure 2 : Work procedures workflow

Table 2 : The synthesized Panchromatic (PAN)

PAN No.	method	References
PAN 1	Landsat 9 PAN band (15 m) original landsat9 PAN band	
PAN 2	1st Independent component analysis (ICA) novelly synthesis	[73]
PAN 3	Non-negative matrix factorization (NMF) novelly synthesis	[34, 35]
PAN 4	Gram-Schmidt transformation (GST) novelly synthesis	[36, 74]
PAN 5	B2 of Sent 2 (blue) selected	[15]
PAN 6	B3 of Sent 2 (green) selected	
PAN 7	B4 of Sent 2 (red) selected	
PAN 8	B8 of Sent 2 (NIR) selected	
PAN 9	Average of (B2, B3, B4, and B8) synthesis	[75]
PAN 10	Weight average of (B2, B3, B4, and B8) based on (r)'s &ς of sen2 bands novelty synthesis	Equation 2&3

Three pan-sharpening algorithms were utilized: Gram-Schmidt (GS), Principal Components Analysis (PC), and the Nearest Neighbor Diffusion (NN) method. To evaluate the sharpening process, the original Landsat-9 image was resampled from 30 to 10 m due to the absence of a reference image. The characteristics of the sharpened images were then measured using seven fidelity criteria listed in Table 3.

Table 3: Fused images evaluation criteria

Criteria	*Equations*	*Ref.*
Root Mean Square Error (RMSE)	$RMSE = \sqrt{\frac{1}{n}\sum_{i=1}^{n}(y_i - \hat{y}_i)^2}$	[37]
Error Relative Globale Adimensionnelle de Synthèse (ERGAS)	$ERGAS = \frac{100}{r} \times \sqrt{\frac{1}{n}\sum_{i=1}^{n}\left(\frac{RMSE_i}{\hat{x}_i}\right)^2}$	[76]
Peak signal-to-noise ratio (PSNR)	$PSNR = 20 \times \log\left(\frac{MAX}{\sqrt{MSE}}\right)_{10}$	[41, 42]
Correlation coefficient (r)	$eq.(2)$	[71]
Structural Similarity Index (SSIM)	$SSIM = \frac{(2\mu_x\mu_y + C_1)(2\sigma_{xy} + C_2)}{(\mu_x^2 + \mu_y^2 + C_1)(\sigma_x^2 + \sigma_y^2 + C_2)}$	[44].
Spectral Angle Mapper (SAM)	$SAM = \arccos\left(\frac{\langle V, V' \rangle}{\| V \| \cdot \| V' \|}\right)$	[77]
Universal image Quality Index (UIQI)	$Q = \frac{4\sigma_{xy}x_{\text{mean}}y_{\text{mean}}}{(\sigma_x^2 + \sigma_y^2)(x_{\text{mean}}^2 + y_{\text{mean}}^2)} \cdot \frac{2\sigma_{xy}}{\sigma_x^2 + \sigma_y^2} \cdot \frac{2x_{\text{mean}}y_{\text{mean}}}{x_{\text{mean}}^2 + y_{\text{mean}}^2}$	[45, 78]

A classification process was conducted on the resulting images using supervised classification algorithms, the support vector machine (SVM) with three kernels: linear (LIN), radial basis functions (RBF), polynomial (POL), and maximum likelihood (ML). This involved identifying classes, selecting training sets through a field survey, studying the satellite scenes, and utilizing high-resolution images available for the study area.

3. Results and discussions

To increase the spatial resolution of Landsat 9 from 30 to 10 m, the procedures outlined in Table 2 were implemented. Dimensionality reduction techniques were employed successfully to derive bands PAN2, PAN3, and PAN4, while bands PAN5, PAN6, PAN7, and PAN8 were directly obtained from the four Sentinel-2A bands. Additionally, eq.1 was utilized to generate PAN9. To compute PAN10, the Correlation Coefficient (r) between the Landsat bands and the four Sentinel bands was calculated, as detailed in Table 4. The results show that band 4 correlates highest with the Landsat 9 bands.

Table 4 : The (r) values of LSBs and SB

LS9 bands	SB_2	SB_3	SB_4	SB_8
LSB_1	0.824234	0.84186	0.88247	0.37102
LSB_2	0.84998	0.86327	0.88915	0.35166
LSB_3	0.85622	0.87853	0.88698	0.35886
LSB_4	0.82714	0.8522	0.90232	0.37936
LSB_5	0.25726	0.29547	0.36012	0.88036
LSB_6	0.68926	0.71595	0.80495	0.626463
LSB_7	0.77124	0.784214	0.84939	0.44034
AVERAGE (r)	0.725048	0.747356	0.796483	0.486866

Table 5 the, standard deviation (s) values for the four Sentinel bands, as presented in Table 5, were utilized to determine weights for each band according to equations 3 and 4 and those specified in Table 6.

Table 5 : The s values of 10 Sentinel 2 bands

Band No.	B2	B3	B4	B8
s value	0.02599227	0.03046747	0.03923006	0.0374608

Table 6: Bands weight values of PAN 10

Band No.	B2	B3	B4	B8
Normalized band weight	0.2018199	0.24717545	0.33562403	0.21538063

Table 7 displays the correlation coefficient (r) values between the synthesized panchromatic (PAN) bands and Landsat 9 bands (LSBs), highlighting the correlation strengths. The PAN10, PAN2, and PAN9 panchromatic bands (10 m) exhibit the highest correlation coefficients with LSB bands, suggesting their reliability. Conversely, PAN8, which represents the IR band (842 nm), demonstrates the lowest (r) value, indicating a weaker correlation, and this result is expected because this wavelength registers information that differs from most of the Landsat-9 bands (except LSB_5). These findings serve as valuable indicators of the efficacy of the synthesized panchromatic bands.

Table 7: (r) values of synthesized PAN bands and landsat9 bands (LSBs)

PAN Bands No.	LSB_1	LSB_2	LSB_3	LSB_4	LSB_5	LSB_6	LSB_7	Average
PAN1 (15m)	0.93019	0.94520	0.94977	0.9469	0.34621	0.8222	0.88734	0.83255
PAN2	0.84552	0.851425	0.85682	0.86028	0.544162	0.838005	0.83011	0.803761
PAN3	0.77232	0.771829	0.778751	0.785924	0.687766	0.84118	0.780263	0.774006
PAN4	0.77214	0.77157	0.778317	0.78572	0.687018	0.840875	0.78011	0.773679
PAN5	0.82423	0.84998	0.85622	0.827149	0.257267	0.689267	0.77124	0.725051
PAN6	0.84186	0.86327	0.878534	0.8522	0.29547	0.715956	0.78421	0.747357
PAN7	0.88247	0.88915	0.886987	0.902321	0.36012	0.804951	0.84939	0.796484
PAN8	0.37102	0.35166	0.35886	0.37936	0.88036	0.62646	0.44034	0.486866
PAN9	0.83155	0.83777	0.84458	0.84486	0.56938	0.83473	0.81883	0.797386
PAN10	0.84875	0.854902	0.860096	0.863658	0.53504	0.837015	0.832125	0.804513

In assessing the fused images using the Gram-Schmidt (GS) method, the results listed in Table 8 align consistently with previous results in Table 7. Notably, the fused images that rely on PAN10, PAN2, and PAN9 exhibit superior values across various evaluation criteria. This underscores the significance of these panchromatic bands in the fusion process.

Table 8 : The GS evaluation results

Fused images	RMSE	SAM	ERGAS	PSNR	SSIM	UIQI	(r)
ideal values	0	NAN	0	INF	1	1	1
GS PAN1	0.0974	15.9057	7.7036	20.2267	0.7248	0.8322	0.7928
GS PAN2	0.0379	6.7273	3.3229	28.4371	0.9565	0.9787	0.9614
GS PAN3	0.0414	7.4946	3.6379	27.6506	0.9520	0.9744	0.9537
GS PAN4	0.0402	7.1493	3.5347	27.9002	0.9531	0.9758	0.9563
GS PAN5	0.0524	9.3769	4.5970	25.6179	0.9391	0.9592	0.9262
GS PAN6	0.0490	8.7718	4.3045	26.1891	0.9413	0.9642	0.9353
GS PAN7	0.0409	7.2269	3.5875	27.7716	0.9514	0.9750	0.9551
GS PAN8	0.0735	13.3143	6.4482	22.6787	0.9040	0.9200	0.8544
GS PAN9	0.0387	6.9139	3.3989	28.2408	0.9558	0.9780	0.9596
GS PAN10	0.0378	6.7174	3.3197	28.4455	0.9564	0.9788	0.9615

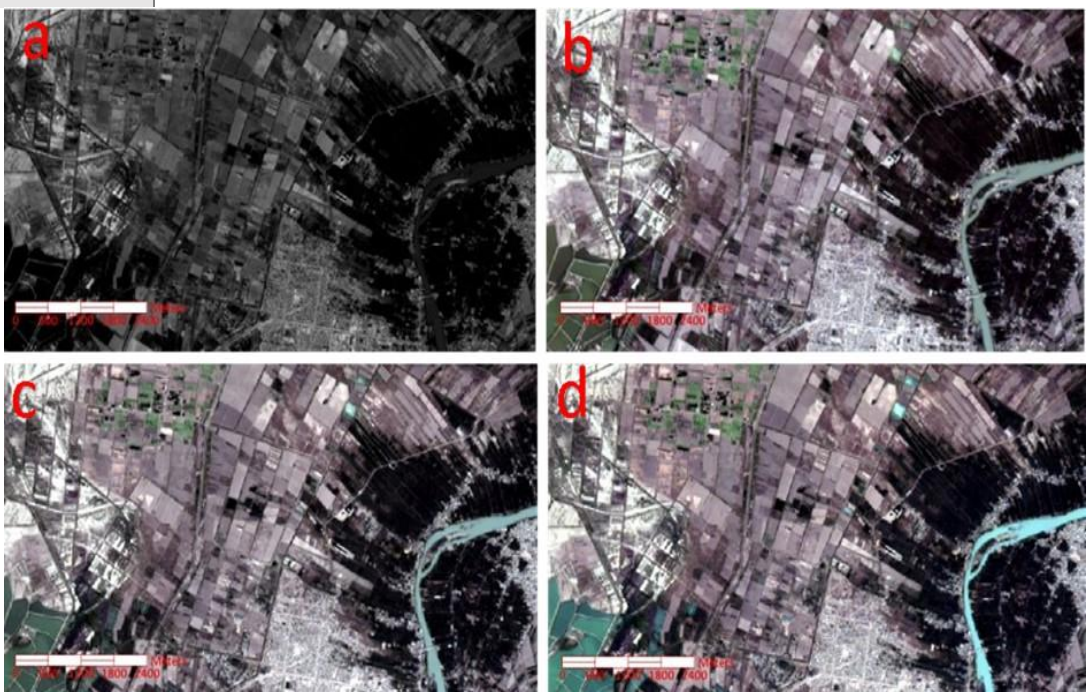

Figure 3: a) PAN1 (15m), b) GS PAN1, c) PC PAN1, and d) NN PAN1.

The evaluation of fused images by principal component sharpening (PC) values reflects the outcomes obtained from the GS method, albeit with a slight enhancement. This improvement can be attributed to the inherent common principles of both methods, particularly their reliance on component substitution (CS). The pivotal role played by the panchromatic band in influencing outcomes is evident in the closely aligned results of both approaches. As can be seen in both subjective (Figures 3, 4, 5, and 6 in the sub-figures a, b, and c) and objective evaluation (Tables 8 and 9), both GS and PC are highly affected by the PAN bands' qualities. Figures (3-6) show a sub-image of the study area (Figure 1b), which was selected to present the results of the work methods.

Table 9: PC evaluation results

Fused images	RMSE	SAM	ERGAS	PSNR	SSIM	UIQI	(r)
ideal values	0	NAN	0	INF	1	1	1
PC PAN1	0.098943	16.1924	7.8238	20.0922	0.71403	0.8260	0.78479
PC PAN2	0.037403	6.65463	3.2831	28.5417	0.95668	0.9791	0.96237
PC PAN3	0.041527	7.51446	3.6450	27.6333	0.951116	0.9743	0.95362
PC PAN4	0.039684	7.04414	3.4833	28.0275	0.95354	0.9765	0.95764
PC PAN5	0.051622	9.23403	4.53124	25.7431	0.939621	0.96033	0.928329
PC PAN6	0.048241	8.6229	4.23437	26.3317	0.941848	0.96535	0.937412
PC PAN7	0.039642	7.0026	3.47966	28.0367	0.95244	0.97660	0.957735
PC PAN8	0.074026	13.4146	6.49775	22.6122	0.901595	0.9184	0.852621
PC PAN9	0.038423	6.8733	3.37269	28.3079	0.955714	0.97802	0.960294
PC PAN10	0.037328	6.63459	3.27655	28.5591	0.956694	0.97925	0.962525

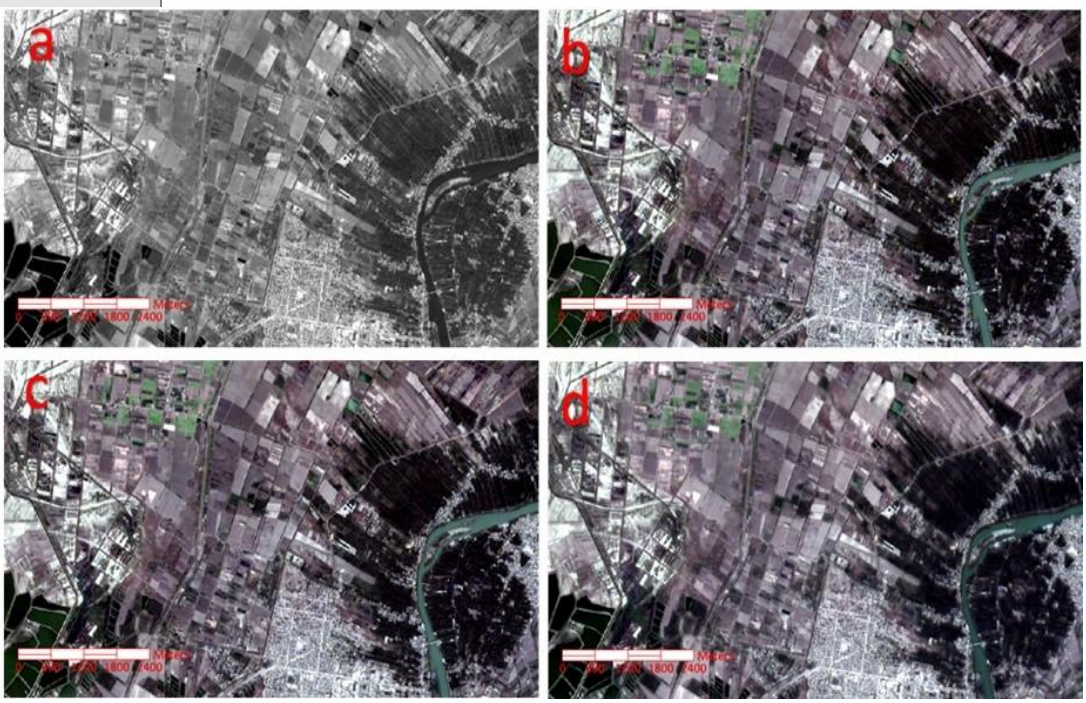

Figure 4: a)PAN2, b) GS PAN2, c) PC PAN2, and d) NN PAN2.

However, the objective assessment of fused images using the nearest neighbor diffusion (NN) method (Table 10) yields noticeably different results than previous methodologies. The fused image based on the original Landsat panchromatic band PAN1(15m) gives higher evaluation values in comparison with the images that were fused using the GS and PC methods in all assessment criteria results, except the results of the SSIM and UIQI were both indices contain information that measures the luminance, contrast, and structure which gives lower values and this consists with the finding in [66]. Furthermore, PAN8 is the preferred choice for achieving optimal fused image quality (objectively) despite its lower (r) value than the original Landsat 9, as shown in Figure 5. It can be seen in the results of NN methods that there is less consistency between the subjective and objective evaluations; most of the fused images show very good visual but give lower values in the results of objective evaluations (Figures 3, 4, 5, and 6 in the subfigures a and d). The other important note is that the results of this method are less affected by the PAN band quality from the previous methods (GS and PC). One possible explanation for why the NN method

exhibits less sensitivity to the quality of the PAN bands is that the NN method can learn the optimal weights for combining the source images. In contrast, the GS and PC methods rely on fixed mathematical transformations that may not capture the salient features of the images [79]. This discrepancy in results underscores the importance of considering diverse evaluation metrics and the nuanced impact of individual bands on overall image quality.

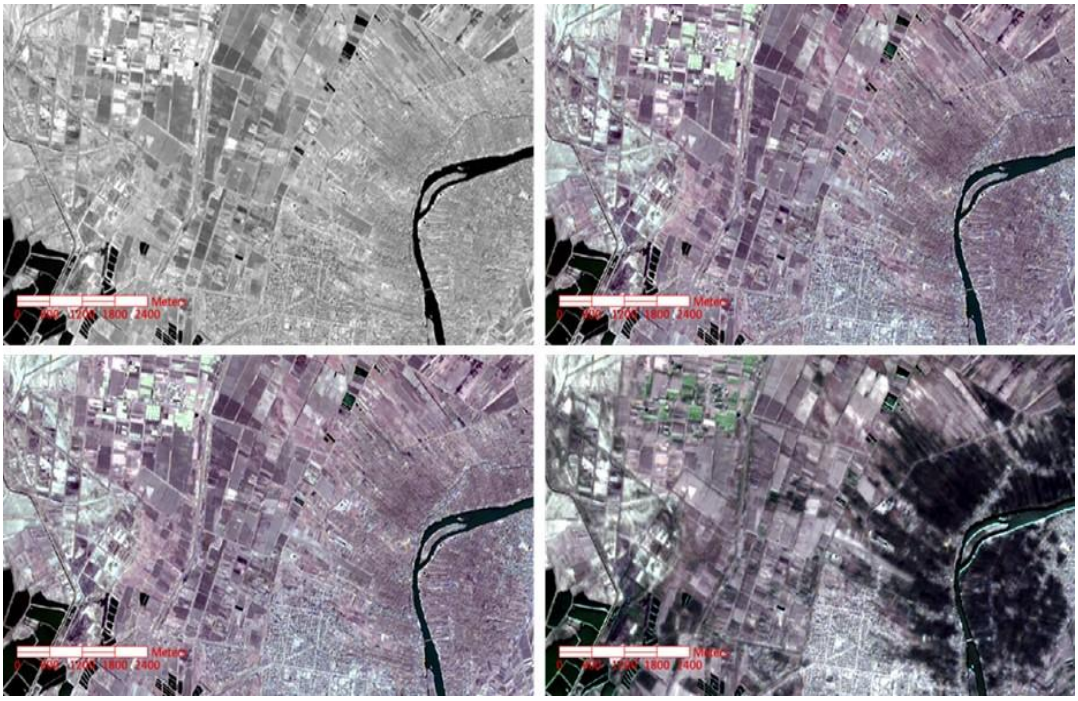

Figure 5: a) PAN8, b) GS PAN8, c) PC PAN8, and d) NN PAN8.

Table 10: The NN evaluation results

Fused image	RMSE	SAM	ERGAS	PSNR	SSIM	UIQI	(r)
ideal values	0	NAN	0	INF	1	1	1
NN PAN1	0.08306	12.8215	6.56831	21.6115	0.69556	0.7965	0.838107
NN PAN2	0.062959	7.8332	5.52636	24.0187	0.91493	0.958229	0.953399
NN PAN3	0.05412	6.82690	4.75047	25.3327	0.93196	0.968627	0.963367
NN PAN4	0.071548	8.72892	6.28022	22.9080	0.89775	0.94705	0.945029
NN PAN5	0.052037	8.98150	4.56766	25.6736	0.93824	0.963134	0.93757
NN PAN6	0.086952	10.6973	7.63235	21.2143	0.86039	0.922088	0.922281
NN PAN7	0.075604	11.5279	6.63624	22.4290	0.87465	0.934446	0.909568
NN PAN8	0.039160	6.61411	3.43737	28.1429	0.94971	0.979148	0.964738
NN PAN9	0.062618	7.59075	5.49641	24.0659	0.91700	0.959102	0.955926
NN PAN10	0.063498	7.92711	5.57363	23.9447	0.91363	0.957477	0.952435

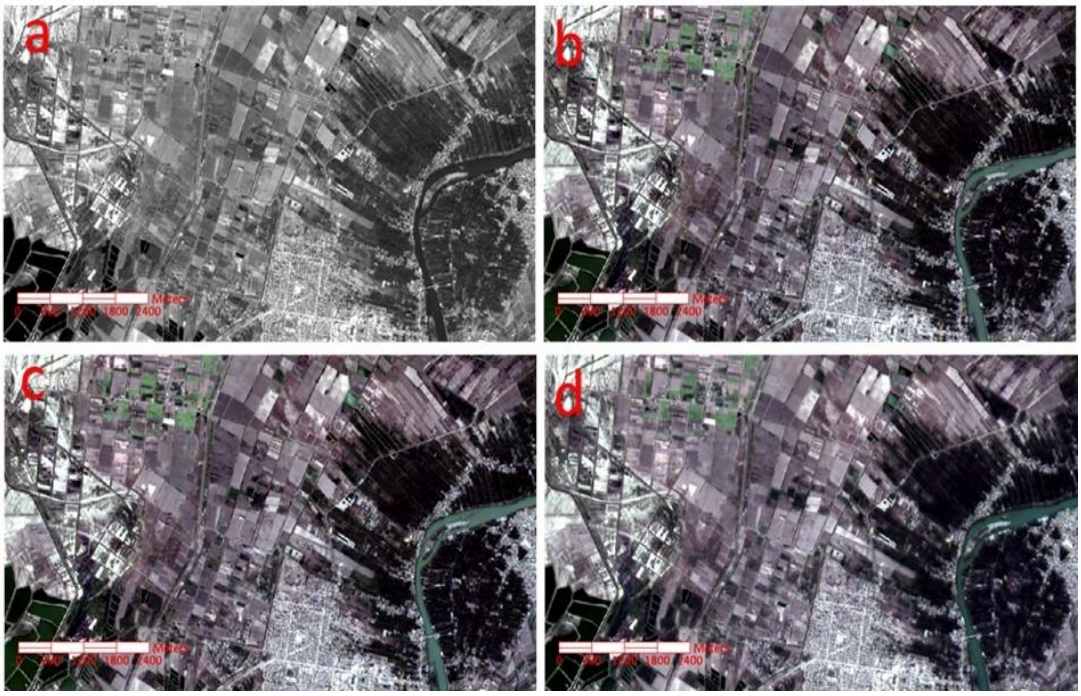

Figure 6: a) PAN10 (10M), b) GS PAN10, c) PC PAN10, and d) NN PAN10.

Upon comparing the classification results (Table 11 and Figure 7) of Landsat-9 (30 m) with those sharpened based on the panchromatic band PAN1 of the Landsat satellite (15m), slightly close overall accuracy (OA) values were found. Notably, there is a slight increase in (OA) when employing the Support Vector Machine (RBF) classifier with images sharpened using the Gram-Schmidt method. These (OA) results align with the results of Komeil Rokni [80], which shows a minor increase with images fused using PC and classified with a Maximum likelihood (ML) classifier. Conversely, other results indicate a slight decrease in Overall Accuracy (OA) results. The results generally do not exhibit statistically significant changes due to the increase in spatial resolution from 30 to 15 m [81]. This could be attributed to the positive effect of increasing the spatial resolution, which is counterbalanced by a parallel negative effect resulting from the deterioration in the spectral properties of the sharpened images [79], mainly since broad features characterize the study area. Changes in accuracy will have a positive impact limited to small areas, especially on the boundaries separating features and small residential clusters scattered between agricultural areas. However, the negative effect of spectral degradation may extend over more expansive areas, which results in some incorrect classifications of these features in other places.

These results are expected for several reasons, the most significant of which is that the spectral range of the panchromatic PAN1 band does not cover all wavelengths of the fused images [82, 83]. Hence, this increases the possibility of spectral degradation of the bands located within the near IR spectrum as well as SWIR, as the Panchromatic band PAN1 of the Landsat 9 satellite extends within part of the visible spectrum only (503-675) nm [68]. In addition to that, there is generally spectral deterioration due to sharpening operations. The initial evaluation (visually) of the classification results of Landsat-9 images (30 m) shows that the identifications of classes have been done well (except for the regions in the borders between the classes). This is due to two factors, the first of which is the high radiometric resolution of the satellite, and the second is the high separation ability of the support vector machine algorithm, which gave better results compared to the maximum likelihood classifier. In statistical evaluation, a clear superiority in the classification of fused image results is

found, especially with the two-component substitution algorithms. By comparing the outcomes of supervised classification for fused images derived from the synthesis and selected panchromatic bands (PAN) of the Sentinel-2 satellite's four 10 m bands, it is evident that classification accuracy notably increases when employing component substitution algorithms across most PAN bands. However, an exception is observed with PAN 8, which corresponds to the near-infrared (NIR) band (842 nm) of Sentinel-2.

Interestingly, the classification results for PAN 8 images yielded Overall Accuracy (OA) values lower than those obtained from classifying the original images at a spatial resolution of 30 meters. These results align with the objective evaluations outlined in Tables 8 and 9. Despite the lower (OA), PAN 8 images demonstrated advantages in separating specific classes. They were particularly helpful in distinguishing between natural vegetation, crops, trees, and palm classes[84]. This suggests that PAN 8 might contain valuable information for specific classification tasks, even if it does not necessarily improve overall accuracy. The infrared band (PAN 8) registers information about vegetation health, water content, and thermal properties. This information might be highly relevant for specific classes like crops and trees [85] and give lower misclassification between the built-up and bare lands, but it might not be well-integrated with other bands during fusion, leading to lower overall accuracy.

Conversely, other fused images demonstrated varying increases in accuracy, with some reaching up to 9.6%, as in SVM with RBF kernel coupled with PC PAN10 image. These results are consistent with previous research reported by Mateen, S. et al. [86], who observed improved land cover classification OA by fusing Sentinel-2 and Landsat-8 images using a Gram-Schmidt algorithm. Mansourmoghaddam, M. et al. [57] also found that fusing Landsat-8 data with the 10 m Sentinel-2 bands can increase land cover classification accuracy by up to 10% compared to using the original Landsat-8 dataset. The enhanced spatial resolution enables the classifiers to capture the spectral signatures of these fine-grained features more effectively. This observation is consistent with Sigurdsson J. et al. [58], who mentioned enhanced accuracy in classifying small features by fusing Landsat-8 and Sentinel-2 images. This was mainly observed in images sharpened using the panchromatic bands PAN2, PAN3, PAN4, PAN9, and PAN10. These findings agree with the image quality assessments provided in Table 8&9.

Furthermore, the superiority of Support Vector Machine (SVM) classifiers, particularly those employing the (RBF) kernel, is evident across all fused images RBF kernel, which is consistent with the results of [56]. On the other hand, using the Maximum Likelihood classifier resulted in slight accuracy increases for most images within the component substitution category. The low values of the (OA) when using the ML classifiers result from the false separation between closely spectral classes, especially the bare lands and built-up [87], and between the green classes [88].

The (OA) results of the SVM classifier were better than the ML classifier, which is compatible with the results of [60], [65], [89], and [90].

When employing the Nearest Neighbor Diffusion (NN) algorithm for image fusion, noticed marginal improvements in overall accuracy (OA) when coupled with SVM classifiers across various images, particularly those fused with PAN5, PAN9, and PAN10. However, integration with the Maximum Likelihood classifier results in slight decreases in OA across all fused images via the NN method. Although these images generally exhibit more aesthetically pleasing characteristics than those produced by alternative fusion algorithms,

they are less conducive to classification processes. This disparity may stem from the NN method's fundamental principle, which involves estimating the pixel value in the pan-sharpened image by aggregating information from its nearest neighbors in the PAN image. These neighbors contribute to the final pixel value based on assigned weights, reflecting the spectral influence of each neighbor [91, 92], which may affect the actual spectral signature of the pixels depending on their neighbors' pixels. The classification results of (NN) need further investigation to overcome the cones of this algorithm results.

Overall, the results highlight the effectiveness of used approaches like dimension reduction and weight ratio methods in extracting simulated panchromatic bands (PANs), especially PAN10 (weighted average), PAN2 (ICA), and PAN9 (average) bands. Leveraging these bands to sharpen Landsat-9 satellite images via component substitution algorithms proves efficient.

In classification, PAN10 stands out in GS SVM LIN, achieving the highest OA at 86.08%, closely followed by PAN2 at 85%. In PC SVM RBF, PAN9 and PAN10 exhibit the highest OA at 87.8% and 88.04%, respectively. GS SVM RBF identifies PAN10 as the top performer, with an OA of 87.75%. Meanwhile, in PC MAXLIK, PAN2 and PAN6 tie for the highest OA at 82.5%. These findings underscore the critical role of specific panchromatic bands in improving classification accuracy and the superiority of the SVM across diverse fusion methods. Component substitution algorithms prove effective, particularly considering the computational efficiency of these methods. Additionally, the results suggest the feasibility of utilizing Band 3 (PAN6) of the Sentinel-2 satellite to sharpen Landsat-9 data for land cover classification.

Table 11 : Overall accuracy (OA) of the original and fused image classification **%.**

Classifiers	***LS30 m***	***PAN 1***	***PAN 2***	***PAN 3***	***PAN 4***	***PAN 5***	***PAN 6***	***PAN 7***	***PAN 8***	***PAN 9***	***PAN10***
GS SVM LIN		79.73	85	83.5	83.5	82.4	85.7	82.8	76.25	82.6	86.08
PC SVM LIN	80.65	78.77	85	84.8	84.5	81.9	85.8	83.6	76.74	85.5	85.04
NN SVM LIN		79.74	81.2	81.3	81.5	82.4	81.2	79.5	78.59	82.3	80.77
GS SVM RBF		79.51	87.9	86.9	85.9	83	86.5	83.9	75.74	83.5	87.75
PC SVM RBF	78.44	78.79	87.8	86.9	85.6	82.9	86.3	84.4	75.96	87.8	88.04
NNSVM RBF		78.68	80.8	81.4	80.8	81.9	80.4	79.7	80.18	82	81.02
GS SVM PO		79.85	87	84.7	84.6	82.5	86.5	83	75.7	83.4	87.06
PC SVM PO	80.25	78.82	86.9	86	84.9	82.8	86.4	83.8	76.22	87.4	87.04
NNSVM PO		79.62	81.1	81.8	81.9	82.3	80.7	79.8	79.62	82	80.72
GS MAXLIK		75.24	81.5	81.2	81.8	81.6	82.5	81.5	77.41	80	81.58
PC MAXLIK	79.9	80.7	81.5	81.1	81.35	81.8	82.5	81.5	77.29	81.6	81.59
NN MAXLIK		78.32	79.7	79.8	79.1	77.4	78.9	78.4	78.28	79.6	79.59

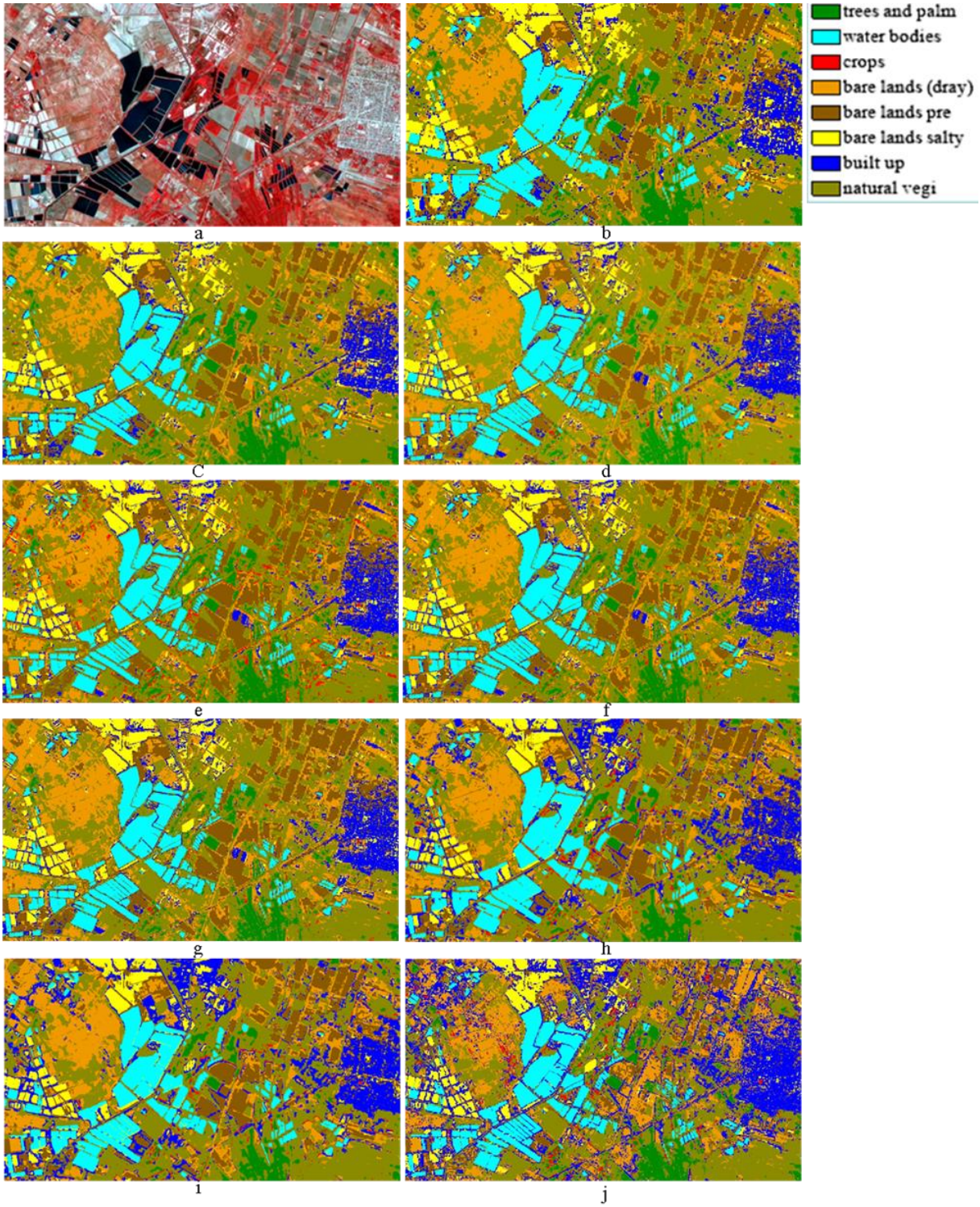

Figure 7: a) false color RGB (543) (GS PAN2), b) SVM LIN (LS 30 M), c) SVM POLY (GSPAN1), d) SVM RBF (GSPAN2), e) SVM RBF (GSPAN9), f) SVM RBF (PC PAN2), g) SVM RBF(PCPAN10), h) SVM LIN (NNPAN5), i) SVM LIN (NNDPAN9), and j) MAXLIK (PCPAN6).

4. Conclusions

The novelty adopted methods that employed the data reduction algorithms and the weighted averages successfully extracted the synthesized panchromatic (PAN) bands from the four 10 m bands of the sentinel-2 MSI satellite to sharpen the Landsat 9 OLI 2 bands. The evaluation results of the fused images and their classification accuracy results show that the

components substitutions (GS and PC) fusion algorithms outperform the (NN) algorithm in both objective assessments of the fused images and the classification (OA) results. Some results of the synthetic PAN bands (PAN10, PAN2, PAN9, and PAN 6) showed superior image fusion and classification process performance. In contrast, the visual assessment shows better results. The lowest classification (OA) has resulted from the selected PAN8 band in all classifiers, although it has some advantages in separation between vegetation classes and between the built-up and bare lands, making it essential in some classification applications. That suggests it might contain valuable information for specific classification tasks, even if it does not necessarily improve overall accuracy. The results also highlight the importance of choosing the right panchromatic band and fusion algorithm for specific applications. Through the classification results presented in Table 11, the SVM classifiers were shown to be more robust to the variations introduced by different fusion methods. The NN fusion results were reasonably acceptable, but further investigation is needed to understand its limitations and potential improvements in the method. This study provides a strategy for improving spatial resolution and land cover classification using all available remote sensing data.

References

[1] X. Liu *et al.*, "Classifying urban land use by integrating remote sensing and social media data," *International Journal of Geographical Information Science,* vol. 31, no. 8, pp. 1675-1696, 2017.

[2] A. S. Mahdi, "The Land Use and Land Cover Classification on the Urban Area," *Iraqi Journal of Science,* vol. 63, pp. 4609-4619, 2022

[3] E. F. Lambin, M. D. A. Rounsevell, and H. J. Geist, "Are agricultural land-use models able to predict changes in land-use intensity?," *Agriculture, Ecosystems & Environment,* vol. 82, no. 1, pp. 321-331, 2000/12/01/ 2000.

[4] L. K. Abbas, "Mapping Land Cover/Land Use for Change Derivation Using Remote Sensing and GIS Technique," *Iraqi Journal of Science,* pp. 3772-3778, 2021.

[5] F. Waldner, S. Fritz, A. Di Gregorio, and P. Defourny, "Mapping priorities to focus cropland mapping activities: Fitness assessment of existing global, regional and national cropland maps," *Remote Sensing,* vol. 7, no. 6, pp. 7959-7986, 2015.

[6] Z. R. Ali and A. S. Muhaimeed, "The study of temporal changes on land cover/land use prevailing in Baghdad governorate using RS & GIS," *The Iraqi Journal of Agricultural Sciences,* vol. 47, no. 3, pp. 846-855, 2016.

[7] J. W. Chipman, T. M. Lillesand, J. E. Schmaltz, J. E. Leale, and M. J. Nordheim, "Mapping lake water clarity with Landsat images in Wisconsin, USA," *Canadian Journal of remote sensing,* vol. 30, no. 1, pp. 1-7, 2004.

[8] M. Niroumand-Jadidi, F. Bovolo, M. Bresciani, P. Gege, and C. Giardino, "Water Quality Retrieval from Landsat-9 (OLI-2) Imagery and Comparison to Sentinel-2," *Remote Sensing,* vol. 14, no. 18, p. 4596, 2022.

[9] E. Micijevic *et al.*, *Radiometric performance of the Landsat 9 Operational Land Imager over the first 8 months on orbit* (SPIE Optical Engineering + Applications). SPIE, 2022.

[10] M. J. Choate, R. Rengarajan, J. C. Storey, and M. Lubke, "Landsat 9 Geometric Characteristics Using Underfly Data," *Remote Sensing,* vol. 14, no. 15, p. 3781, 2022.

[11] M. A. Wulder *et al.*, "Fifty years of Landsat science and impacts," *Remote Sensing of Environment,* vol. 280, p. 113195, 2022.

[12] Q. Wang *et al.*, "Fusion of Landsat 8 OLI and Sentinel-2 MSI Data," *IEEE Transactions on Geoscience and Remote Sensing,* vol. 55, no. 7, pp. 3885-3899, 2017.

[13] D. Phiri, M. Simwanda, S. Salekin, V. R. Nyirenda, Y. Murayama, and M. Ranagalage, "Sentinel-2 data for land cover/use mapping: A review," *Remote Sensing,* vol. 12, no. 14, p. 2291, 2020.

[14] V. B. ESA, Z. Szantoi, and F. Gascon, "Copernicus Sentinel-2 Mission: Calibration and Validation activities," *GSICS Q,* vol. 14, no. 1, 2020.

[15] Q. Wang, W. Shi, Z. Li, and P. M. Atkinson, "Fusion of Sentinel-2 images," *Remote Sensing of Environment,* vol. 187, pp. 241-252, 2016/12/15/ 2016.

[16] K. Siok, I. Ewiak, and A. Jenerowicz, "Multi-Sensor Fusion: A Simulation Approach to Pansharpening Aerial and Satellite Images," *Sensors (Basel),* vol. 20, no. 24, p. 7100, Dec 11 2020.
[17] V. P. Shah, N. H. Younan, and R. L. King, "An efficient pan-sharpening method via a combined adaptive PCA approach and contourlets," *IEEE Transactions on geoscience and remote sensing,* vol. 46, no. 5, pp. 1323-1335, 2008.
[18] P. Ghamisi *et al.*, "Multisource and multitemporal data fusion in remote sensing: A comprehensive review of the state of the art," *IEEE Geoscience and Remote Sensing Magazine,* vol. 7, no. 1, pp. 6-39, 2019.
[19] J. R. Townshend, C. O. Justice, C. Gurney, and J. McManus, "The impact of misregistration on change detection," *IEEE Transactions on Geoscience and remote sensing,* vol. 30, no. 5, pp. 1054-1060, 1992.
[20] H. M. Abduljabbar, "Satellite Images Fusion Using Modified PCA Substitution Method," *Ibn AL-Haitham Journal For Pure and Applied Sciences,* vol. 30, no. 1, pp. 29-37, 2017.
[21] L. Wald, T. Ranchin, and M. Mangolini, "Fusion of satellite images of different spatial resolutions: Assessing the quality of resulting images," *Photogrammetric engineering and remote sensing,* vol. 63, no. 6, pp. 691-699, 1997.
[22] F. A. Hadi and R. A. Abdulwahab, "Hyperspectral Image Sharpening Using Fusion Techniques-A Case Study at Salah Al-Din Province/Iraq," *Iraqi Journal of Science,* 2024.
[23] C. Thomas, T. Ranchin, L. Wald, and J. Chanussot, "Synthesis of Multispectral Images to High Spatial Resolution: A Critical Review of Fusion Methods Based on Remote Sensing Physics," *IEEE Transactions on Geoscience and Remote Sensing,* vol. 46, no. 5, pp. 1301-1312, 2008.
[24] G. Vivone *et al.*, "A critical comparison among pansharpening algorithms," *IEEE Transactions on Geoscience and Remote Sensing,* vol. 53, no. 5, pp. 2565-2586, 2014.
[25] I. J. Muhsin and K. H. Salih, "Enhancement and Quality Assessment of Multi-Spectral Image Using Different Fusion Methods," *Iraqi Journal of Science,* vol. 56, no. 1A, pp. 257-264, 2015.
[26] R. A. Abdulwahab, L. A. Al-Ani, and A. H. Shaban, "Fused images based on division of hyperspectral images into spectral groups," in *AIP Conference Proceedings*, 2023, vol. 3018, no. 1: AIP Publishing.
[27] V. K. Shettigara, "A generalized component substitution technique for spatial enhancement of multispectral images using," 1992.
[28] T. Maurer, "How to pan-sharpen images using the gram-schmidt pan-sharpen method–A recipe," *Int. Arch. Photogramm. Remote Sens. Spatial Inf. Sci.,* 2013.
[29] H. R. Shahdoosti and H. Ghassemian, "Combining the spectral PCA and spatial PCA fusion methods by an optimal filter," *Information Fusion,* vol. 27, pp. 150-160, 2016.
[30] V. Karathanassi, P. Kolokousis, and S. Ioannidou, "A comparison study on fusion methods using evaluation indicators," *International Journal of Remote Sensing,* vol. 28, no. 10, pp. 2309-2341, 2007.
[31] W. Sun, B. Chen, and D. Messinger, "Nearest-neighbor diffusion-based pan-sharpening algorithm for spectral images," *Optical Engineering,* vol. 53, no. 1, p. 013107, 2014.
[32] Snehmani, A. Gore, A. Ganju, S. Kumar, P. Srivastava, and H. R. RP, "A comparative analysis of pansharpening techniques on QuickBird and WorldView-3 images," *Geocarto International,* vol. 32, no. 11, pp. 1268-1284, 2017.
[33] G. Ortaç and G. Özcan, "A Comparative Study for Hyperspectral Data Classification with Deep Learning and Dimensionality Reduction Techniques," *Uludağ University Journal of The Faculty of Engineering,* vol. 23, no. 3, pp. 73-90, 2018.
[34] D. E. Holmes and L. C. Jain, *Data Mining: Foundations and Intelligent Paradigms: Volume 1: Clustering, Association and Classification*. Springer Science & Business Media, 2011.
[35] N. Lopes and B. Ribeiro, "Non-Negative Matrix Factorization (NMF)," in *Machine Learning for Adaptive Many-Core Machines - A Practical Approach*, N. Lopes and B. Ribeiro, Eds. Cham: Springer International Publishing, 2015, pp. 127-154.
[36] Y. Bian, "A Gram–Schmidt process based approach for improving DEA discrimination in the presence of large dimensionality of data set," *Expert Systems with Applications,* vol. 39, no. 3, pp. 3793-3799, 2012/02/15/ 2012.

[37] P. Jagalingam and A. V. Hegde, "A Review of Quality Metrics for Fused Image," *Aquatic Procedia,* vol. 4, pp. 133-142, 2015/01/01/ 2015.
[38] M. Q. Kaittan, "Improve the Spatial Resolution of Multispectral Satellite Image using Different Image Sharpening Techniques," *Iraqi Journal of Science,* pp. 227-232, 2018.
[39] L. Alparone, L. Wald, J. Chanussot, C. Thomas, P. Gamba, and L. M. Bruce, "Comparison of pansharpening algorithms: Outcome of the 2006 GRS-S data-fusion contest," *IEEE Transactions on Geoscience Remote Sensing,* vol. 45, no. 10, pp. 3012-3021, 2007.
[40] T. Ranchin and L. Wald, "Fusion of high spatial and spectral resolution images: The ARSIS concept and its implementation," *Photogrammetric engineering and remote sensing,* vol. 66, no. 1, pp. 49-61, 2000.
[41] V. Naidu, "Discrete cosine transform based image fusion techniques," *Journal of Communication, Navigation and Signal Processing,* vol. 1, no. 1, pp. 35-45, 2012.
[42] D. Poobathy and R. M. Chezian, "Edge detection operators: Peak signal to noise ratio based comparison," *I.J. Image, Graphics and Signal Processing,* vol. 10, pp. 55-61, 2014.
[43] A. A. N. Al-Jasim, T. A. Naji, and A. H. Shaban, "The Effect of Using the Different Satellite Spatial Resolution on the Fusion Technique," *Iraqi Journal of Science,* pp. 4131-4141, 2022.
[44] C. Pohl and J. Van Genderen, *Remote sensing image fusion: A practical guide*. Crc Press, 2016.
[45] W. Zhou and A. C. Bovik, "A universal image quality index," *IEEE Signal Processing Letters,* vol. 9, no. 3, pp. 81-84, 2002.
[46] C. Pohl and J. Van Genderen, "Review article multisensor image fusion in remote sensing: concepts, methods and applications," *International Journal of Remote Sensing,* vol. 19, no. 5, pp. 823-854, 1998.
[47] T. A. Naji and A. J. Hatem, "New adaptive satellite image classification technique for al Habbinya region west of Iraq," *Ibn AL-Haitham Journal For Pure and Applied Sciences,* vol. 26, no. 2, pp. 143-149, 2017.
[48] M. Romaszewski, P. Głomb, and M. Cholewa, "Semi-supervised hyperspectral classification from a small number of training samples using a co-training approach," *ISPRS Journal of Photogrammetry and Remote Sensing,* vol. 121, pp. 60-76, 2016.
[49] H. Abduljabbar and T. Naji, "SEPARATING THE TERRAIN COVER OF IRAQI MARSHES REGION USING NEW SATELLITE BAND COMBINATION," *Iraqi Journal of Agricultural Sciences,* vol. 51, no. 6, 2020.
[50] S. M. De Jong and F. D. Van der Meer, *Remote sensing image analysis: including the spatial domain*. Springer Science & Business Media, 2007.
[51] M. Pal and G. M. Foody, "Feature selection for classification of hyperspectral data by SVM," *IEEE Transactions on Geoscience and Remote Sensing,* vol. 48, no. 5, pp. 2297-2307, 2010.
[52] J. Su, D. Yi, C. Liu, L. Guo, and W.-H. Chen, "Dimension Reduction Aided Hyperspectral Image Classification with a Small-sized Training Dataset: Experimental Comparisons," *Sensors,* vol. 17, no. 12, p. 2726, 2017.
[53] T. Zhang, J. Su, C. Liu, W. H. Chen, H. Liu, and G. Liu, "Band selection in sentinel-2 satellite for agriculture applications," in *23rd International Conference on Automation Computing*, 2017, pp. 1-6.
[54] T. D. Pham, J. Xia, N. T. Ha, D. T. Bui, N. N. Le, and W. Takeuchi, "A review of remote sensing approaches for monitoring blue carbon ecosystems: Mangroves, seagrasses and salt marshes during 2010–2018," *Sensors,* vol. 19, no. 8, p. 1933, 2019.
[55] J. Hogland, N. Billor, and N. Anderson, "Comparison of standard maximum likelihood classification and polytomous logistic regression used in remote sensing," *European Journal of Remote Sensing,* vol. 46, no. 1, pp. 623-640, 2013.
[56] Y. Bouslihim, M. H. Kharrou, A. Miftah, T. Attou, L. Bouchaou, and A. Chehbouni, "Comparing pan-sharpened Landsat-9 and sentinel-2 for land-use classification using machine learning classifiers," *Journal of Geovisualization and Spatial Analysis,* vol. 6, no. 2, p. 35, 2022.
[57] M. Mansourmoghaddam, I. Rousta, H. Ghaffarian, and M. H. Mokhtari, "Evaluating the capability of spatial and spectral fusion in land-cover mapping enhancement," *Earth Observation and Geomatics Engineering,* vol. 6, no. 1, pp. -, 2022.

[58] J. Sigurdsson, S. E. Armannsson, M. O. Ulfarsson, and J. R. Sveinsson, "Fusing sentinel-2 and Landsat 8 satellite images using a model-based method," *Remote Sensing,* vol. 14, no. 13, p. 3224, 2022.
[59] P. Thanh Noi and M. Kappas, "Comparison of Random Forest, k-Nearest Neighbor, and Support Vector Machine Classifiers for Land Cover Classification Using Sentinel-2 Imagery," *Sensors,* vol. 18, no. 1, p. 18, 2018.
[60] R. H. Topaloğlu, E. Sertel, and N. Musaoğlu, "Assessment of classification accuracies of Sentinel-2 and Landsat-8 data for land cover/use mapping," *The International archives of the photogrammetry, remote sensing and spatial information sciences,* vol. 41, pp. 1055-1059, 2016.
[61] M. A. Raheem and A. J. Hatem, "Calculation of Salinity and Soil Moisture indices in south of Iraq-Using Satellite Image Data," *Energy Procedia,* vol. 157, pp. 228-233, 2019.
[62] I. J. Al-Rubiey, "Increase the intelligibility of multispectral image using pan-sharpening techniques for many remotely sensed images," *Ibn AL-Haitham Journal For Pure and Applied Sciences,* vol. 28, no. 3, 2017.
[63] A. J. Hatem, A. A. N. Al-Jasim, and H. M. Abduljabbar, "A study of the climate and human impact on the future survival of the Al-Sannya marsh in Iraq," *Journal of Water and Land Development,* pp. 168-173-168-173, 2021.
[64] M. Majed, H. M. AbdulJabbar, and A. Sciences, "The Change in the Land Cover of Mahmudiyah City in Iraq for the Last Three Decades," *Ibn Al-Haitham Journal for Pure and Applied Sciences,* vol. 35, no. 3, pp. 44-55, 2022.
[65] B. Rimal, S. Rijal, and R. Kunwar, "Comparing support vector machines and maximum likelihood classifiers for mapping of urbanization," *Journal of the Indian Society of Remote Sensing,* vol. 48, pp. 71-79, 2020.
[66] R. A. Abdulwahab, L. A. Al-Ani, and A. H. Shaban, "Hyperspectral pansharpening improvement using MNF transformation," in *AIP Conference Proceedings*, 2023, vol. 3018, no. 1: AIP Publishing.
[67] D. A. Maciel *et al.*, "Validity of the Landsat surface reflectance archive for aquatic science: Implications for cloud-based analysis," *Limnology and Oceanography Letters,* vol. 8, no. 6, pp. 850-858, 2023.
[68] J. G. Masek *et al.*, "Landsat 9: Empowering open science and applications through continuity," *Remote Sensing of Environment,* vol. 248, p. 111968, 2020/10/01/ 2020.
[69] E. ESA, "Sentinel-2 user handbook," *Sentinel-2 User Handbook,* p. 64, 2015.
[70] M. A. Z. Aguilera, "Classification Of Land-Cover Through Machine Learning Algorithms For Fusion Of Sentinel-2a And Planetscope Imagery," in *2020 IEEE Latin American GRSS & ISPRS Remote Sensing Conference (LAGIRS)*, 2020, pp. 246-253: IEEE.
[71] S. Li, J. T. Kwok, and Y. Wang, "Using the discrete wavelet frame transform to merge Landsat TM and SPOT panchromatic images," *Information Fusion,* vol. 3, no. 1, pp. 17-23, 2002.
[72] Y. Zhou, A. Mayyas, and M. A. Omar, "Principal Component Analysis-Based Image Fusion Routine with Application to Automotive Stamping Split Detection," *Research in Nondestructive Evaluation,* vol. 22, no. 2, pp. 76-91, 2011/03/31 2011.
[73] L. Liu, C.-f. Li, Y.-m. Lei, J.-y. Yin, and J.-j. Zhao, "Feature extraction for hyperspectral remote sensing image using weighted PCA-ICA," *Arabian Journal of Geosciences,* vol. 10, pp. 1-10, 2017.
[74] H. Wang, B. Yi, and M. Ye, "Variable selection based on principal basis analysis," *Journal of Beijing University of Aeronautics Astronautics,* vol. 34, no. 11, p. 1288, 2008.
[75] M. Selva, B. Aiazzi, F. Butera, L. Chiarantini, and S. Baronti, "Hyper-sharpening: A first approach on SIM-GA data," *IEEE Journal of selected topics in applied earth observations and remote sensing,* vol. 8, no. 6, pp. 3008-3024, 2015.
[76] L. Wald, *Data fusion: definitions and architectures: fusion of images of different spatial resolutions*. Presses des MINES, 2002.
[77] H. Li, L. Jing, and Y. Tang, "Assessment of pansharpening methods applied to WorldView-2 imagery fusion," *Sensors,* vol. 17, no. 1, p. 89, 2017.
[78] Z. Shao, J. Cai, P. Fu, L. Hu, and T. Liu, "Deep learning-based fusion of Landsat-8 and Sentinel-2 images for a harmonized surface reflectance product," *Remote Sensing of Environment,* vol. 235, p. 111425, 2019/12/15/ 2019.

[79] R. Ducay and D. Messinger, *Hyperspectral-multispectral image fusion using nearest-neighbor diffusion-based sharpening algorithm* (SPIE Defense + Commercial Sensing). SPIE, 2022.
[80] K. Rokni, "Investigating the impact of Pan Sharpening on the accuracy of land cover mapping in Landsat OLI imagery," *Geodesy and Cartography,* vol. 49, no. 1, pp. 12–18-12–18, 2023.
[81] H. Pi-Fuei, L. C. Lee, and C. Nai-Yu, "Effect of spatial resolution on classification errors of pure and mixed pixels in remote sensing," *IEEE Transactions on Geoscience and Remote Sensing,* vol. 39, no. 12, pp. 2657-2663, 2001.
[82] G. He, S. Xing, Z. Xia, Q. Huang, and J. Fan, "Panchromatic and multi-spectral image fusion for new satellites based on multi-channel deep model," *Machine Vision Applications,* vol. 29, pp. 933-946, 2018.
[83] T. Ngigi, E. Nduati, W. Xianhu, and M. Götza, "Perspective Chapter: Mix-Unmix Pan-Sharpener–Novel Pan-Sharpening Method Based on Mixing Constituent Multispectral Bands and Unmixing Panchromatic Band," in *Digital Image Processing - Latest Advances and Applications*, C. Dr. Francisco Javier, Ed. Rijeka: IntechOpen, 2024.
[84] T. A. Naji, "Implementation of remote sensing for vegetation studying using vegetation indices and automatic feature space plot," *Journal of Natural Sciences Research,* vol. 5, no. 10, pp. 94-108, 2015.
[85] Y. Liu, W. Gong, X. Hu, and J. Gong, "Forest Type Identification with Random Forest Using Sentinel-1A, Sentinel-2A, Multi-Temporal Landsat-8 and DEM Data," *Remote Sensing,* vol. 10, no. 6, p. 946, 2018.
[86] S. Mateen, N. Nuthammachot, K. Techato, and N. Ullah, "Billion Tree Tsunami Forests Classification Using Image Fusion Technique and Random Forest Classifier Applied to Sentinel-2 and Landsat-8 Images: A Case Study of Garhi Chandan Pakistan," *ISPRS International Journal of Geo-Information,* vol. 12, no. 1, p. 9, 2023.
[87] V. S. Bramhe, S. K. Ghosh, and P. K. Garg, "EXTRACTION OF BUILT-UP AREA BY COMBINING TEXTURAL FEATURES AND SPECTRAL INDICES FROM LANDSAT-8 MULTISPECTRAL IMAGE," *Int. Arch. Photogramm. Remote Sens. Spatial Inf. Sci.,* vol. XLII-5, pp. 727-733, 2018.
[88] B. R. Shivakumar and S. V. Rajashekararadhya, "Spectral similarity for evaluating classification performance of traditional classifiers," in *2017 International Conference on Wireless Communications, Signal Processing and Networking (WiSPNET)*, 2017, pp. 1999-2004.
[89] S. John and A. O. Varghese, "Analysis of support vector machine and maximum likelihood classifiers in land cover classification using Sentinel-2 images," *Proceedings of the Indian National Science Academy,* vol. 88, no. 2, pp. 213-227, 2022/06/01 2022.
[90] M. H. Kesikoglu, U. H. Atasever, F. Dadaser-Celik, and C. Ozkan, "Performance of ANN, SVM and MLH techniques for land use/cover change detection at Sultan Marshes wetland, Turkey," *Water Science and Technology,* vol. 80, no. 3, pp. 466-477, 2019.
[91] W. Sun, B. Chen, and D. Messinger, "Nearest-neighbor diffusion-based pan-sharpening algorithm for spectral images," *Optical Engineering,* vol. 53 no. 1, p. 013107, 2014.
[92] J. Zhao, L. Huang, H. Yang, D. Zhang, Z. Wu, and J. Guo, "Fusion and assessment of high-resolution WorldView-3 satellite imagery using NNDiffuse and Brovey algorithms," in *2016 IEEE International Geoscience and Remote Sensing Symposium (IGARSS)*, 2016, pp. 2606-2609.